PHOTONICS Research

Active control of terahertz quasi-BIC and asymmetric transmission in a liquid-crystal-integrated metasurface

Shi-Tong Xu,[1,2,3] Junxing Fan,[2,4] Zhanqiang Xue,[2] Tong Sun,[1] Guoming Li,[1] Jiandi Li,[1] Dan Lu,[2] and Longqing Cong[2,5]

[1]Shandong Provincial Key Laboratory of Laser Polarization and Information Technology, School of Physics and Engineering, Qufu Normal University, Qufu 273165, China
[2]Department of Electrical and Electronic Engineering, Southern University of Science and Technology, Shenzhen 518055, China
[3]e-mail: xustonenk@163.com
[4]e-mail: fanjx@sustech.edu.cn
[5]e-mail: conglq@sustech.edu.cn

Received 5 June 2024; revised 13 July 2024; accepted 20 July 2024; posted 23 July 2024 (Doc. ID 531952); published 25 September 2024

Quasi-bound states in the continuum (quasi-BICs) offer an excellent platform for the flexible and efficient control of light-matter interactions by breaking the structural symmetry. The active quasi-BIC device has great application potential in fields such as optical sensing, nonlinear optics, and filters. Herein, we experimentally demonstrate an active terahertz (THz) quasi-BIC device induced by the polarization conversion in a liquid crystal (LC)-integrated metasurface, which consists of a symmetrically broken double-gap split ring resonator (DSRR), an LC layer, and double graphite electrodes. In the process of LC orientation control under the external field, the device realizes the active control from the OFF state to the ON state. In the OFF state, the LC has no polarization conversion effect, and the device behaves in a non-resonant state; but for the ON state, the device exhibits obvious quasi-BIC resonance. Furthermore, we achieve asymmetric transmission based on polarization-induced quasi-BIC modulation precisely at the quasi-BIC resonance position, and its isolation can be controlled by the external field. The study on dynamic quasi-BIC by the LC-integrated metasurface introduces a very promising route for active THz devices, which guarantees potential applications for THz communications, switching, and sensing systems.

https://doi.org/10.1364/PRJ.531952

1. INTRODUCTION

Terahertz (THz, 1 THz $= 10^{12}$ Hz) waves, typically covering 0.1–10 THz, occupy the transitional region of the electromagnetic spectrum between electronics and photonics [1]. THz technology has garnered significant attention due to its unique characteristics and potential applications in imaging, non-destructive testing, biomedicine, and next-generation wireless communications [2–5]. The burgeoning development of THz technology is impossible without the breakthrough of THz functional devices, such as THz modulators [6,7], polarization converters [8,9], isolators [10,11], filters [12,13], and switches [14,15]. The performance of these devices commonly depends on the strength of light-matter interactions, which manifest as a high-quality (Q) factor resonance. However, natural materials usually enable a relatively weak interaction with THz radiations, and the devices are severely limited by the large volume and losses.

The concept of bound states in the continuum (BICs) has attracted considerable attention in optics and photonics, owing to their infinite photon lifetime and Q-factors in theory [16–24]. BICs show great promise for enhancing light-matter interactions, and they have been widely studied in optical sensing, nonlinear optics, and filters [25–29]. However, BIC is a state whose energy is completely bound to the resonant system and thus uncouples to free space. There are two typical categories of BIC, one is symmetry-protected BIC and the other is accidental BIC [30,31]. By breaking the symmetry of the structure, the symmetry-protected BIC shifts to a leaky mode with limited Q-factor and resonant bandwidth, which is called a quasi-BIC [32–34]. Metamaterials provide a reliable platform for the study of quasi-BIC, and different types of unit cells have been found to support quasi-BIC, such as circular and square split ring resonators [17,35], tilted elliptic strip pairs [36,37], and nanodisks with holes [38]. In our previous work, Cong and Singh [39] demonstrated dual BICs in a symmetry-protected square split ring metamaterial, and the quasi-BIC is experimentally observed in the THz spectrum by slightly breaking the C2 symmetry with large Q-factors. Nevertheless, once the structural parameters of these BICs or quasi-BICs are determined, it is difficult to realize the active control of the device.

Recently, active control of optical resonances has been highly desired in various THz application scenarios, such as THz sensing, switching, and wireless communications. The incorporation of the tunable materials with metamaterial or metasurfaces provides an efficient approach for achieving active THz quasi-BIC devices. The active control mechanism is mainly attributed to perturbations induced by phase transition, change of electrical conductivity, or refractive index, which are induced by external stimuli. Tunable functional materials can fill in gaps of resonators or be designed directly as metamaterials, including graphene [21,40,41], phase-transition materials [42,43], and semiconductors [44–48]. For example, Hu *et al.* [49] reported a BIC-mediated reconfigurable metamaterial for spatiotemporal lineshape tailoring, and the symmetry of the structure was broken by introducing VO_2 into the split ring resonators. Dynamic control of the device was realized under optical pumping. In particular, the LC possesses large birefringence and low absorption loss in the THz regime, and its orientation can be actively controlled by the external electric field, magnetic field, or light field, which is a very promising active material in the THz band. Nowadays, the LC-based metasurface has attracted extensive attention for its superiority in flexible control of electromagnetic waves [50–52].

In this work, we experimentally demonstrate an LC-integrated metasurface for THz quasi-BIC modulation and asymmetric transmission induced by polarization conversion. The quasi-BIC resonance is supported by an asymmetric double-gap split ring resonator, but behaves as a non-resonant state in the orthogonal polarization excitation. Therefore, we could switch on and off the quasi-BIC by manipulating the incident polarization of THz waves. Here, we propose a configuration of an LC-integrated metasurface, where dynamic polarization rotation is realized by the LC layer actuated by an external voltage. Furthermore, our proposed LC-integrated metasurface is capable of asymmetric transmission with the active isolation degree by changing the external field. This work provides a new paradigm for active quasi-BIC devices, which could be applied to THz communication, switching, and sensing systems.

2. STRUCTURE DESIGN

The radiation properties of BIC have been thoroughly studied in recent works from symmetry and reciprocal space of the unit cells. It is indeed helpful to understand the intrinsic properties of BIC or quasi-BIC; however, the radiation will be fixed once the structure is fabricated. An effective strategy is thus necessary to tune the mode properties, and polarization offers an external freedom. We propose an LC-integrated metasurface supporting quasi-BIC where LC layers play the role of polarization controller. Figure 1(a) shows the schematic diagram of the configuration where the LC layer is actuated by two graphite electrodes. A constant magnetic field (M-field) is applied along the u-axis to anchor the LC molecules, so that the orientation control of LC molecules is possible in the u–z plane with the electric field along the z-axis.

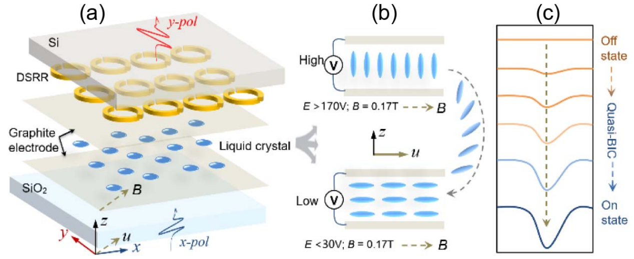

Fig. 1. (a) Schematic diagram of liquid crystal (LC)-integrated quasi-BIC metasurface. Here LC is filled into the cell between two graphite electrodes, and a static magnetic field pre-anchors LC molecules along the u-axis. (b) Schematic diagram of LC orientation evolution with actuation between low and high voltages. (c) Active modulation of quasi-BIC from OFF to ON states due to polarization rotation enabled by LC layer.

The working principles of the LC layer and tunable quasi-BIC are shown in Figs. 1(b) and 1(c). LC molecules will be driven by an external electric field along the z-axis when the actuation voltage is higher than the threshold, and gradually shifted back to the x-y plane along the M-field direction with an intermediate state when the actuation voltage decreases. The shift of LC molecule orientation will lead to the modulation of the polarization state of light transmitting through the layer. With a high voltage, incident polarization conserves due to the isotropic response of the LC layer, while the polarization state is rotated by 90° without external electrical actuation. The polarization rotation will lead to the switch ON and OFF states of quasi-BIC whose response is polarization dependent. As manifested from the schematic diagram of the transmission spectra, the quasi-BIC resonances will experience the modulation in Fig. 1(c).

3. RESULTS AND DISCUSSION

A. Experimental Results of Quasi-BIC and LC Birefringence

Figure 2(a) shows a unit cell of the proposed metallic metasurface, which is a typical subwavelength double-gap split ring resonator (DSRR). Here, DSRR was fabricated by traditional photolithography, and it has a uniform period of $p = 73$ μm; the inside diameter of the circular ring is $r = 25$ μm, the width is $d = 5$ μm, and the gap is $g = 3$ μm. In particular, we define an angle α representing the degree of asymmetry, and $\alpha = 0°$ means the open ring is located in the middle of the DSRR, in which case the BIC mode of symmetry protection is supported. The photonic band and analysis of the BIC mode can be found in Appendix A. The transition from BIC to quasi-BIC resonance is realized by breaking the C2 symmetry of the structure with the increased α. Under y-polarization excitation, the BIC to quasi-BIC responses of DSRR with different α were obtained, and the experimental and simulated THz transmission spectra are shown in Fig. 2(b) and Fig. 2(c), respectively. In order to observe quasi-BIC more easily in experiments, we chose a relatively large asymmetric breaking angle here. An obvious Fano resonance in the THz spectra was observed with

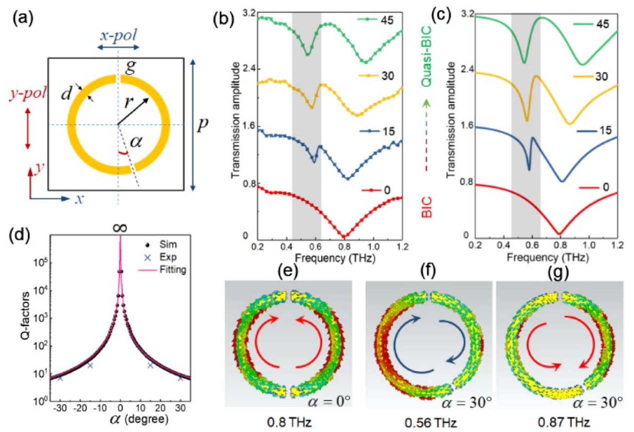

Fig. 2. (a) Schematic diagram of DSRR as a building block of a metasurface array. (b) Experimental and (c) simulated transmission amplitude spectra of DSRR with different rotation angles of 0°, 15°, 30°, and 45° under *y*-polarization excitations. (d) *Q*-factors of quasi-BIC with α. Surface current distributions of (e) DSRR with $\alpha = 0°$ at 0.8 THz, DSRR with $\alpha = 30°$ located at (f) 0.56 THz and (g) 0.87 THz, and the arrows indicate the direction of the surface current.

α of 15°, 30°, and 45°, while the resonance cannot be captured for symmetric structure with $\alpha = 0°$. The experimental results match well with the simulations. A standard THz time-domain spectral (THz-TDS) system was employed to conduct the THz experiments. The detailed experiments and device fabrication procedures can be found in Appendix B and Appendix C. The numerical simulations were carried out based on the finite element method using commercially available software (COMSOL Multiphysics). In simulations, the silicon substrate was modeled as a lossless material with a permittivity of 11.7. The metallic part of DSRR was set as a perfect electrical conductor (PEC) to calculate the eigenmode and radiative *Q*-factors, and modeled as aluminum with a conductivity of 3.56×10^7 S/m for the frequency-domain solver. Periodic boundary conditions were set in the *x*- and *y*-directions, while the *z*-direction was set as a perfectly matched layer (PML).

Based on the analysis of the eigenmode in the simulations, the *Q*-factors of the quasi-BIC were extracted in Fig. 2(d). According to Ref. [53], the total Q_{tot} can be decomposed into the radiative Q_{rad} and resistive Q_{res}, which follows as Q_{tot} ($1/Q_{\mathrm{tot}} = 1/Q_{\mathrm{rad}} + 1/Q_{\mathrm{res}}$). Here, the total Q_{tot} equals Q_{res} for the DSRR modeled as PEC without the resistive loss, and it shows a clear diverging trend to infinity at $\alpha = 0°$. The extracted *Q*-factors have a good match with the theoretical fitting of the inverse square equation. According to the Fano lineshape equation, the experimental Q_{tot} can be obtained from the transmission spectra in Fig. 2(b), but the experimental value of *Q*-factors is lower than the simulations due to the extra contribution of both radiative and non-radiative losses. In addition, we show the surface current distributions of DSRR with different asymmetry degrees in Figs. 2(e)–2(g). Under the *y*-linear polarization excitations, the current distribution of the two arms of DSRR ($\alpha = 0°$) is symmetrical with equal intensity and reversed direction, and then it is an obvious dipole resonance mode [36]. For the DSRR with $\alpha = 30°$, a Fano resonance appears at 0.56 THz with annular current distribution and symmetry-broken intensity [Fig. 2(f)], which allows a channel to couple with the incident radiation (quasi-BIC). In addition, the current distribution at 0.8 THz presents an inverted but asymmetric intensity distribution, as shown in Fig. 2(g). As a result, the quasi-BIC mode was achieved by the symmetry breaking in DSRR, and the evolution can be clarified from the surface current distributions.

The birefringence characteristics of the independent LC layer were experimentally probed with external actuation of electric and magnetic fields [54], as illustrated in Fig. 3(a). Here, we adopted the LC named NC-M-LC-LDn03 (Nanjing Ningcui Optical Technology Co., Ltd.) with a thickness of 1 mm. The adjustable voltage is applied through graphite electrodes. The graphite layer has a thickness of 2.4 μm, and it has a high transmission of nearly 90% [52], so the graphite electrode has little impact on the overall transmittance of the device. A constant *M*-field of 0.17 T is applied to uniformly orient the LC molecules. We measured the THz time-domain spectra when LC is oriented along the *y*-axis or *z*-axis, and the effective refractive index of n_e and n_o can be achieved under the *y*-linear polarization incidence. Figure 3(b) shows the time-domain spectra with different LC orientations, and the LC-*y* signal lags significantly behind that of LC-*z*. Based on the Fourier transform of the time-domain signal, we obtain the refractive index of $n_o = 1.53$ and $n_e = 1.81$, as well as the phase difference spectrum as shown in Fig. 3(c). A specific phase difference of $\Delta\varphi = \pi$ was realized at 0.56 THz.

Due to the limitations of the experimental THz testing system, it is difficult to capture the BIC modes with extremely high *Q*-factors; therefore we choose the symmetry-broken DSRR with $\alpha = 30°$ as the basic quasi-BIC structure in the following discussion. The microscope image of DSRR is presented in Fig. 3(d). To illustrate the effect of polarization conversion in the LC-integrated metasurface, the transmittance spectra of DSRR under two orthogonal polarizations are given in Figs. 3(e) and 3(f). Different from the Fano resonance that

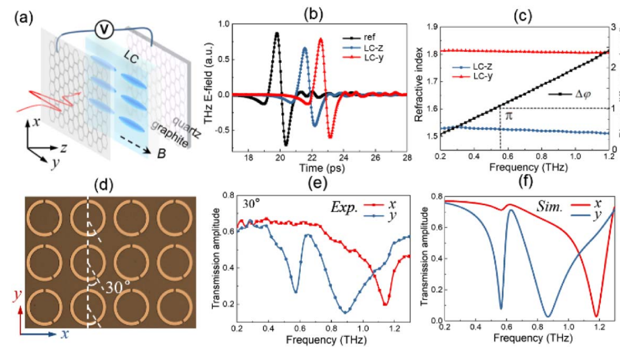

Fig. 3. (a) Schematic diagram of LC birefringence measurement under electric (*z*-axis) and magnetic fields (*y*-axis). (b) Experimental time-domain signals when LC orients along the *y*-axis and *z*-axis, and double quartz layer without LC as the reference. (c) Experimental LC refractive indexes and phase difference. (d) Microscope image of quasi-BIC structure with an angle $\alpha = 30°$. (e) Experimental and (f) simulated transmission amplitude spectra of quasi-BIC structure at *x*-pol and *y*-pol excitations.

occurs at 0.56 THz and supports a quasi-BIC mode, DSRR under x-polarization behaves as a non-resonant spectrum at this frequency (0.56 THz), which brings the possibility of switching quasi-BIC induced by the LC polarization conversion.

B. Active Control of Quasi-BIC in LC-Integrated Metasurface

To analyze the polarization-induced THz quasi-BIC modulation in an LC-integrated metasurface, the experimental setup was designed with two polarizers, as shown in Fig. 4(a). The first polarizer P_1 was fixed to ensure that the incident light is linear polarization along the x-axis, while the second polarizer P_2 can be rotated to detect the parallel polarization component (T_{xx}) and the crossed polarization component (T_{yx}). Here, T_{ij} stands for the polarization components of the i-polarized output induced by j-polarized incidence ($i, j = x, y$). Figures 4(b) and 4(c) illustrate the working principle of polarization state conversion and induced resonance in the decomposed structure of an LC-integrated metasurface. In the case when LC is along the z-axis driven by the high voltage, LC has no polarization conversion effect on the incident light, and the device appears as a non-resonant state (at 0.56 THz) output from DSRR in Fig. 4(b), which is consistent with the red line in Fig. 3(e). When an external voltage is switched off, LC is bound to the M-field along the u-axis direction with an angle of 45° relative to incident polarization. Based on classical polarization optics, the polarization state will be converted to y-linear polarization when $\Delta\varphi = \pi$. If the frequency of polarization rotation matches with the quasi-BIC, the quasi-BIC resonance will be excited, which is depicted in Fig. 4(c).

Based on the polarization testing setup, the experimentally measured T_{xx} and T_{yx} under different actuation voltages were obtained as shown in Figs. 4(d)–4(g). At forward incidence [$+z$ direction, expressed as → LC-DSRR →, the same configuration as shown in Fig. 4(a)], the unconverted T_{xx} component first appears as a flat non-resonant state at a high voltage of 170 V, and then drops off with the decreased voltage, finally forming a transmittance valley, as shown in Fig. 4(d). On the contrary, the transformed T_{yx} component gradually increases with the decreased voltage, and it results from the polarization conversion during the LC-orientation changes from the z-axis to the u-axis. Notably, the resonance valley (quasi-BIC state) is still retained in the transmittance spectra, which is consistent with the diagram in Fig. 4(c). Therefore, the active modulation of quasi-BIC is achieved in the LC-integrated metasurface. In addition, we studied the T_{xx} and T_{yx} in the situation of backward incidence ($-z$ direction, expressed as ← LC-DSRR ←) in Figs. 4(f) and 4(g). We can observe that the unconverted T_{xx} component in Fig. 4(f) basically coincides with Fig. 4(d), but the transformed T_{yx} component differs greatly compared with Figs. 4(e) and 4(g). Based on the difference of the converted T_{yx} component in forward and backward incidence, the LC-integrated metasurface is expected to achieve asymmetric transmission. The perturbation in the transmittance spectrum is primarily influenced by the dispersion of the introduced LC material and the machining accuracy of the DSRR metasurface.

C. Asymmetric Transmission in LC-Integrated Metasurface

As mentioned above, the LC-integrated metasurface exhibits completely different T_{yx} transmission spectra between the forward incidence and backward incidence. To clearly illustrate the physical mechanism of asymmetric transmission in the LC-integrated metasurface, here we show the transmission schematic diagram of the device in Figs. 5(a) and 5(b). For the forward incidence, a linear polarization incident along the x-axis will be converted to the cross-polarization along the y-axis at the frequency of $\Delta\varphi = \pi$, and then induces Fano resonance by DSRR, which is shown as the quasi-BIC state in Fig. 5(a). As to the backward incidence, the linear polarization along the x-axis first excites DSRR and appears as a non-resonant state, and then is transmitted through the LC layer, but the polarization conversion of the LC layer does not change the resonance state, only the amplitude modulation. Therefore, a non-resonant spectrum was observed from backward incidence, as shown in Fig. 5(b). The measured transmittance spectra from forward and backward incidence with different voltages are depicted in Figs. 5(c)–5(f). In our design, a voltage

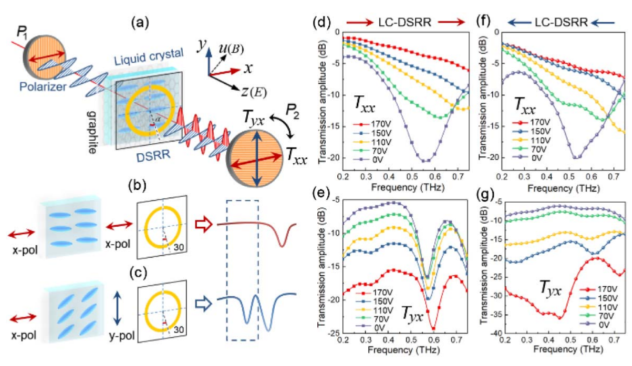

Fig. 4. (a) Schematic diagram of measurement setup for LC-integrated metasurface. The first polarizer (P_1) ensures the incident light is linear polarization along the x-axis, and the transmitted parallel (T_{xx}) and crossed (T_{yx}) polarization components are detected by rotating the second polarizer (P_2). Schematic diagram of polarization state conversion and transmission spectra when LC is along the (b) z-axis and (c) u-axis. Experimentally measured (d) T_{xx} and (e) T_{yx} polarization components under different voltages at forward incidence ($+z$ direction). Experimentally measured (f) T_{xx} and (g) T_{yx} polarization components at backward incidence ($-z$ direction).

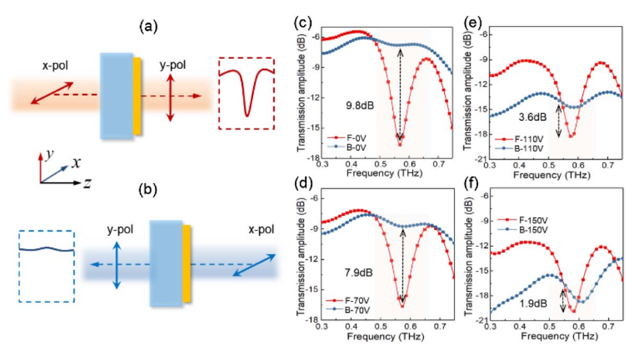

Fig. 5. Analysis of asymmetric transmission of LC-integrated metasurface. Polarization conversion and transmittance spectra at (a) forward incidence and (b) backward incidence. Amplitude transmission (dB) at forward and backward incidence under the voltage of (c) 0 V, (d) 70 V, (e) 110 V, and (f) 150 V.

equal to zero indicates the strongest polarization conversion ability of the LC layer, and the maximal isolation of 9.8 dB is achieved at 0.56 THz when no voltage is applied to the device, as shown in Fig. 5(c). Here, the isolation of asymmetric transmission is defined: $\Delta T_{\text{isolation}} = T_{\text{forward}} - T_{\text{backward}}$. With the increase of voltage, the device gradually loses the polarization conversion effect, which then results in the decrease of asymmetric transmission. The isolation of 1.9 dB is realized when the voltage is 150 V, which could be regarded as symmetric transmission at this state. Therefore, the active control of asymmetric transmission was achieved by adjusting LC orientation under the external field in the LC-integrated metasurface. In this work, the insertion loss of the device primarily originates from the LC layer, and reducing the thickness of the LC layer may result in a decrease in insertion loss. It is possible to adjust the structural parameter of DSRR to a smaller scale to match the thinner LC layer. In addition, the isolation of asymmetric transmission is correlated with the Q-value of the symmetric broken DSRR; therefore, employing a smaller symmetry broken angle with a higher Q-value can effectively enhance device isolation.

4. CONCLUSION

In conclusion, active modulation of quasi-BIC resonance has been experimentally demonstrated through polarization rotation without reconfiguring the structural parameters of resonators. An LC-integrated metasurface was proposed where the LC layer behaves as the polarization conversion and a DSRR metasurface supports a symmetry-broken quasi-BIC resonance. Due to the anisotropic properties of the metasurface, orthogonal polarization of incident light will induce contrasting transmitting responses that form the basis of active modulation via electrically and magnetically actuated LC layers. The combination of polarization rotation and quasi-BIC resonance also enables the asymmetry transmission with a maximal isolation of 9.8 dB between forward and backward incidence, which is also adjustable by external voltage. The isolation of asymmetric transmission of the device can be further improved if a high-Q structure with smaller perturbations is used. Moreover, the metallic metasurface in the composite device also can be substituted by other asymmetry-broken structures. The proposed LC-integrated metasurface configuration offers a powerful platform to study the functional devices in THz applications, which would benefit the next-generation wireless communications and single-pixel imaging.

APPENDIX A: PHOTONIC BAND ANALYSIS OF BIC

Based on the eigenmode analysis in simulations, the photonic band and intrinsic radiative Q of DSRR at $\alpha = 0°$ are depicted in Fig. 6. The eigenmode is excited at y-polarization along the symmetry axes [see Fig. 2(a)], and it possesses the features of a symmetry-protected bound state. The subwavelength DSRR array supports a symmetry-protected BIC with infinite Q-factors at Γ point that are unstable against perturbations of wavevector k. Hence, the introduction of perturbations such as oblique incidence and symmetry breaking in the design

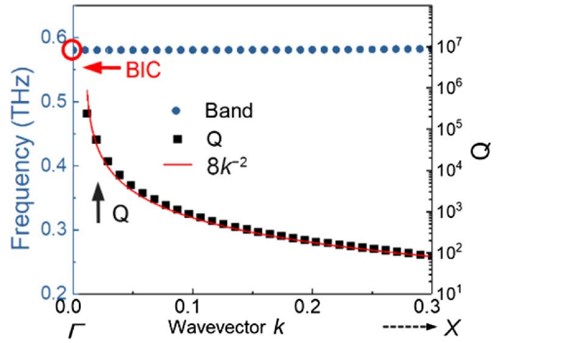

Fig. 6. Band diagram and radiative Q of BIC mode in DSRR ($\alpha = 0°$).

of BIC-metasurfaces enables the achievement of a high Q-factor [55].

APPENDIX B: SAMPLE FABRICATION

The metallic metasurface was fabricated on a 500 μm thick high-resistivity (>10 kΩ · cm) silicon substrate based on conventional lithography. Initially, a 2 μm layer of photoresist (RZJ 304.50) was spin-coated onto the cleaned and polished high-resistance silicon at a speed of 5000 r/s for 30 s, followed by baking at 100°C for 180 s. Subsequently, the DSRR pattern from the mask plate was transferred to the photoresist using conventional ultraviolet lithography (SUSS-MA6) and then developed with the RZX3038 developer for 30 s. The DSRR structure photoresist was removed and the patterned sample was cured by baking it at 120°C for 90 s. Finally, an aluminum layer with a thickness of 200 nm was deposited on the silicon surface through electron beam evaporation (TF500), and any remaining photoresist was eliminated by soaking the sample in acetone solution at a temperature of 60°C for 30 min. For the LC-integrated metasurface, LC is filled between the metallic metasurface and the SiO_2 substrate. To realize the orientation of the electrically controlled LC, the upper and lower surfaces that were directly in contact with the LC were coated with a 2.4 μm thick graphite electrode layer, and the device was finally packaged by UV adhesive.

APPENDIX C: EXPERIMENTAL MEASUREMENT

A commercial terahertz time-domain spectroscopy (THz-TDS) system was employed to conduct the THz experiments at room temperature with humidity at less than 5%. The THz pulse was generated by a low-temperature grown InGaAs/InAlAs photoconductive antenna (PCA), and a detector antenna was used for detection. The excitation source was an erbium-doped fiber laser with a central wavelength of 1550 nm [17]. In our THz-TDS system, the scanning step of the delay line is 5 μm, and the corresponding time interval is 0.033 ps. The scanning range of the experiment is 540 ps and the spectral resolution is 1.83 GHz. To reduce background noise, each experimental data is averaged with 200 scans, and the signal-to-noise ratio of the system is over 90 dB. In addition, a 3D-printed mold is used to hold the NdFeB permanent magnets to apply a static M-field, and the longitudinal voltage is applied by wires that are connected to the front and rear graphite electrodes. The sample is vertically fixed to the hollow aluminum test platform with a pore diameter of 1 cm.

Funding. National Natural Science Foundation of China (62005143, 62175099, 62335011); Basic and Applied Basic Research Foundation of Guangdong Province (2023A1515011085); Shenzhen Science and Technology Innovation Program (20220815151149004, 20230807093617036, JSGGKQTD20221101115656030); Regular Undergraduate University Teacher Visiting and Training Funding of Shandong Province.

Disclosures. The authors declare no conflicts of interest.

Data Availability. Data underlying the results presented in this paper are not publicly available at this time but may be obtained from the authors upon reasonable request.

REFERENCES

1. X. C. Zhang, A. Shkurinov, and Y. Zhang, "Extreme terahertz science," Nat. Photonics **11**, 16–18 (2017).
2. Y. Huang, Y. Shen, and J. Wang, "From terahertz imaging to terahertz wireless communications," Engineering **22**, 106–124 (2023).
3. Z. Y. Yan, L. G. Zhu, K. Meng, *et al.*, "THz medical imaging: from *in vitro* to *in vivo*," Trends Biotechnol. **40**, 816–830 (2022).
4. X. Wu, H. X. Lu, and K. Sengupta, "Programmable terahertz chip-scale sensing interface with direct digital reconfiguration at sub-wavelength scales," Nat. Commun. **10**, 2722 (2019).
5. T. Nagatsuma, G. Ducournau, and C. C. Renaud, "Advances in terahertz communications accelerated by photonics," Nat. Photonics **10**, 371–379 (2016).
6. X. L. Zhao, J. Lou, X. Xu, *et al.*, "Multifield controlled terahertz modulator based on silicon-vanadium dioxide hybrid metasurface," Adv. Opt. Mater. **10**, 2102589 (2022).
7. R. Degl'Innocenti, H. Lin, and M. Navarro-Cía, "Recent progress in terahertz metamaterial modulators," Nanophotonics **11**, 1485–1514 (2022).
8. Y. D. Gong, Z. Zhang, J. X. Tang, *et al.*, "Research progress on terahertz achromatic broadband polarization wave plates," Opt. Laser Technol. **166**, 109633 (2023).
9. S. T. Xu, H. F. Zhang, L. Cong, *et al.*, "Dispersion-compensated terahertz ultra-broadband quarter and half wave plates in a dielectric-metal hybrid metadevice," Adv. Opt. Mater. **12**, 2302696 (2024).
10. D. Zhao, F. Fan, Z. Y. Tan, *et al.*, "Tunable on-chip terahertz isolator based on nonreciprocal transverse edge spin state of asymmetric magneto-plasmonic waveguide," Laser Photonics Rev. **17**, 2200509 (2023).
11. R. Y. Dong, J. Y. Sui, Z. J. Li, *et al.*, "The terahertz isolator and switch based on the nonreciprocal feature of magnetized InSb layered photonic structure," Opt. Laser Technol. **169**, 110004 (2024).
12. P. Pitchappa, A. Kumar, R. Singh, *et al.*, "Electromechanically tunable frequency-agile metamaterial bandpass filters for terahertz waves," Adv. Opt. Mater. **10**, 2101544 (2022).
13. A. Maleki, A. Singh, A. Jaber, *et al.*, "Metamaterial-based octave-wide terahertz bandpass filters," Photonics Res. **11**, 526–532 (2023).
14. P. Pitchappa, A. Kumar, S. Prakash, *et al.*, "Volatile ultrafast switching at multilevel nonvolatile states of phase change material for active flexible terahertz metadevices," Adv. Funct. Mater. **31**, 2100200 (2021).
15. X. Liu, J. Huang, H. Chen, *et al.*, "Terahertz topological photonic waveguide switch for on-chip communication," Photonics Res. **10**, 1090–1096 (2022).
16. L. M. Berger, M. Barkey, S. A. Maier, *et al.*, "Metallic and all-dielectric metasurfaces sustaining displacement-mediated bound states in the continuum," Adv. Opt. Mater. **12**, 2301269, (2024).
17. J. X. Fan, Z. L. Li, Z. Q. Xue, *et al.*, "Hybrid bound states in the continuum in terahertz metasurfaces," Opto-Electron. Sci. **2**, 230006 (2023).
18. G. Xu, H. Xing, Z. Xue, *et al.*, "Recent advances and perspective of photonic bound states in the continuum," Ultrafast Sci. **3**, 0033 (2023).
19. X. Qi, J. Wu, F. Wu, *et al.*, "Observation of maximal intrinsic chirality empowered by dual quasi-bound states in the continuum in a planar metasurface," Photonics Res. **12**, 244–252 (2024).
20. W. Wang, Y. K. Srivastava, T. C. Tan, *et al.*, "Brillouin zone folding driven bound states in the continuum," Nat. Commun. **14**, 2811 (2023).
21. C. Huang, L. Liang, P. Chang, *et al.*, "Terahertz liquid biosensor based on a graphene metasurface for ultrasensitive detection with a quasi-bound state in the continuum," Adv. Mater. **36**, 2310493 (2024).
22. T. C. W. Tan, E. Plum, and R. Singh, "Lattice-enhanced Fano resonances from bound states in the continuum metasurfaces," Adv. Opt. Mater. **8**, 1901572 (2020).
23. W. X. Lim, M. Manjappa, P. Pitchappa, *et al.*, "Shaping high-*Q* planar Fano resonant metamaterials toward futuristic technologies," Adv. Opt. Mater. **6**, 1800502 (2018).
24. D. C. Zografopoulos and O. Tsilipakos, "Recent advances in strongly resonant and gradient all-dielectric metasurfaces," Mater. Adv. **4**, 11–34 (2023).
25. K. Koshelev, Y. Tang, K. Li, *et al.*, "Nonlinear metasurfaces governed by bound states in the continuum," ACS Photonics **6**, 1639–1644 (2019).
26. R. Wang, L. Xu, L. Huang, *et al.*, "Ultrasensitive terahertz biodetection enabled by quasi-BIC-based metasensors," Small **19**, 2301165 (2023).
27. L. Hu, B. Wang, Y. Guo, *et al.*, "Quasi-BIC enhanced broadband terahertz generation in all dielectric metasurface," Adv. Opt. Mater. **10**, 2200193 (2022).
28. L. Carletti, K. Koshelev, C. D. Angelis, *et al.*, "Giant nonlinear response at the nanoscale driven by bound states in the continuum," Phys. Rev. Lett. **121**, 033903 (2018).
29. S. Romano, G. Zito, S. Torino, *et al.*, "Label-free sensing of ultralow-weight molecules with all-dielectric metasurfaces supporting bound states in the continuum," Photonics Res. **6**, 726–733 (2018).
30. X. Zhao, C. Chen, K. Kaj, *et al.*, "Terahertz investigation of bound states in the continuum of metallic metasurfaces," Optica **7**, 1548–1554 (2020).
31. P. Liu, Z. Zhao, Y. Xue, *et al.*, "Governance of Friedrich-Wintgen bound states in the continuum by tuning the internal coupling of meta-atoms," Opt. Lett. **49**, 1301–1304 (2024).
32. X. Zhang, W. Shi, J. Gu, *et al.*, "Terahertz metasurface with multiple BICs/QBICs based on a split ring resonator," Opt. Express **30**, 29088–29098 (2022).
33. Y. Zhou, Z. Guo, X. Zhao, *et al.*, "Dual-quasi bound states in the continuum enabled plasmonic metasurfaces," Adv. Opt. Mater. **10**, 2200965 (2022).
34. L. Wang, Z. Zhao, M. Du, *et al.*, "Tuning symmetry-protected quasi bound state in the continuum using terahertz meta-atoms of rotational and reflectional symmetry," Opt. Express **30**, 23631–23639 (2022).
35. V. A. Fedotov, M. Rose, S. L. Prosvirnin, *et al.*, "Sharp trapped-mode resonances in planar metamaterials with a broken structural symmetry," Phys. Rev. Lett. **99**, 147401 (2007).
36. J. Li, J. Li, C. Zheng, *et al.*, "Spectral amplitude modulation and dynamic near-field displaying of all-silicon terahertz metasurfaces supporting bound states in the continuum," Appl. Phys. Lett. **119**, 241105 (2021).
37. J. Tian, Q. Li, P. A. Belov, *et al.*, "High-*Q* all-dielectric metasurface: super and suppressed optical absorption," ACS Photonics **7**, 1436–1443 (2020).
38. V. R. Tuz, A. Vyacheslav, V. Khardikov, *et al.*, "High-quality trapped modes in all dielectric metamaterials," Opt. Express **26**, 2905–2916 (2018).
39. L. Cong and R. Singh, "Symmetry-protected dual bound states in the continuum in metamaterials," Adv. Opt. Mater. **7**, 1900383 (2019).
40. J. Huang, B. Hu, G. Wang, *et al.*, "BICs-enhanced active terahertz wavefront modulator enabled by laser-cut graphene ribbons," Photonics Res. **11**, 1185–1195 (2023).

41. J. Li, J. Li, C. Zheng, *et al.*, "Free switch between bound states in the continuum (BIC) and quasi-BIC supported by graphene-metal terahertz metasurfaces," Carbon **182**, 506–515 (2021).
42. D. D. Wang, J. K. Tian, T. Ma, *et al.*, "Terahertz modulators based on VO_2-metal hybridized metamaterials for free switching between BIC and quasi-BIC states," Opt. Commun. **551**, 130040 (2024).
43. H. Zhong, T. He, Y. Wang, *et al.*, "Efficient polarization-insensitive quasi-BIC modulation by VO_2 thin films," Opt. Express **32**, 5862–5873 (2024).
44. S. Han, L. Cong, Y. K. Srivastava, *et al.*, "All-dielectric active terahertz photonics driven by bound states in the continuum," Adv. Mater. **31**, 1901921 (2019).
45. N. Karl, P. P. Vabishchevich, S. Liu, *et al.*, "All-optical tuning of symmetry protected quasi bound states in the continuum," Appl. Phys. Lett. **115**, 141103 (2019).
46. X. Yu, F. Li, T. Lang, *et al.*, "Ultrasensitive tunable terahertz lithium niobate metasurface sensing based on bound states in the continuum," Photonics Res. **11**, 2168–2178 (2023).
47. M. Manjappa, A. Solanki, A. Kumar, *et al.*, "Solution-processed lead iodide for ultrafast all-optical switching of terahertz photonic devices," Adv. Mater. **31**, 1901455 (2019).
48. T. C. Tan, Y. K. Srivastava, R. T. Ako, *et al.*, "Active control of nanodielectric-induced THz quasi-BIC in flexible metasurfaces: a platform for modulation and sensing," Adv. Mater. **33**, 2100836 (2021).
49. Y. Hu, M. Tong, S. Hu, *et al.*, "Spatiotemporal lineshape tailoring in BIC-mediated reconfigurable metamaterials," Adv. Funct. Mater. **32**, 2203680 (2022).
50. S. Wang, H. B. Guo, B. W. Chen, *et al.*, "Electrically active terahertz liquid-crystal metasurface for polarization vortex beam switching," Laser Photonics Rev. **18**, 2301301 (2024).
51. C. Chen, S. Chen, Y. Ni, *et al.*, "Liquid crystal metasurface for on-demand terahertz beam forming over 110° field-of-view," Laser Photonics Rev. **18**, 2400237 (2024).
52. S.-T. Xu, F. Fan, Y.-Y. Ji, *et al.*, "Terahertz resonance switch induced by the polarization conversion of liquid crystal in compound metasurface," Opt. Lett. **44**, 2450–2453 (2019).
53. T. Christopoulos, O. Tsilipakos, G. Sinatkas, *et al.*, "On the calculation of the quality factor in contemporary photonic resonant structures," Opt. Express **27**, 14505–14522 (2019).
54. S.-T. Xu, F. Fan, H.-Z. Cao, *et al.*, "Liquid crystal integrated metamaterial for multi-band terahertz linear polarization conversion," Chin. Opt. Lett. **19**, 093701 (2021).
55. K. Koshelev, S. Lepeshov, M. Liu, *et al.*, "Asymmetric metasurfaces with high-Q resonances governed by bound states in the continuum," Phys. Rev. Lett. **121**, 193903 (2018).